Benign Interfacial Iodine Vacancies in Perovskite Solar Cells

Lan-ying Wei,[†,§] Wei Ma,[†,§] Chao Lian,[†] and Sheng Meng*[†,‡]

[†]Beijing National Laboratory for Condensed Matter Physics and Institute of Physics, Chinese Academy of Sciences, Beijing 100190, China

[‡]Collaborative Innovation Center of Quantum Matter, Beijing 100190, China

ABSTRACT: Methylammonium lead iodide (MAPbI$_3$) perovskite solar cells (PSCs) have become the forefront of photovoltaic technologies and attracted intense attention worldwide. MAPbI$_3$ perovskites are mostly in the form of thin films in high-performance MAPbI$_3$ PSCs, and charge transfer and other critical electronic dynamic processes take place at the interfaces of PSCs. The iodine vacancy V$_I$ is thought to play a major role in arousing severe hysteresis in photocurrent-photovoltage scan, which limits industrialization of PSCs. However, the surface and interfacial V$_I$ properties of MAPbI$_3$ PSCs have not been systematically studied. We utilize first-principles method and nonadiabatic electron dynamics simulations to study the structural and electronic properties of V$_I$ at various sites of freestanding MAPbI$_3$ film and the MAPbI$_3$/TiO$_2$ heterojunction. We show that the surface and interfacial V$_I$ are more stable than bulk, in agreement with accumulation of V$_I$ at grain boundaries observed in experiments. The migration of V$_I$ in the perovskite layer under electric field during voltage scans contributes to the anomalous hysteresis in PSCs. V$_I$ at Pb−I layer and MA−I layer are quite different: V$_I$ at MA−I layer are more stable, while V$_I$ defect states at Pb−I layer are more local and weakly covalent bonded. V$_I$ promotes both electronic injection and recombination rates, but overall reduces the power conversion efficiencies (PCE) of PSCs. Nevertheless, interfacial V$_I$ is found to be the least harmful to the PCE of PSCs comparing with random sites in the bulk, contributing to the high PCE of MAPbI$_3$ PSCs.
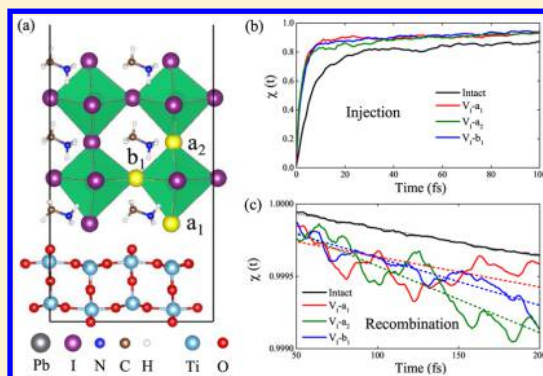
1. INTRODUCTION

To date, the organic−inorganic lead halide perovskite solar cells (PSCs) have reached over 22% power conversion efficiency (PCE).[1,2] Specifically, methylammonium (MA) lead iodide CH$_3$NH$_3$PbI$_3$ (or MAPbI$_3$) PSCs[3−7] have become one of the most promising photovoltaic technologies due to their long carrier diffusion length,[8,9] low recombination rate[10] and large optical absorption coefficient.[11,12] However, despite these fascinating attributes, which are ideal for photovoltaic applications, MAPbI$_3$ PSCs are restricted for extensive industrialization by some critical problems, such as their instabilities against light,[13,14] heat,[15,16] water,[17,18] and the anomalous photocurrent−photovoltage (J−V) hysteresis.[19−22] Previous works demonstrate that the intrinsic defects in MAPbI$_3$ layer, which is ubiquitous and unavoidable, could contribute significantly to the above issues. For example, the ion migration[23−25] and defects induced charge trapping and detrapping mechanisms[26−28] are believed to be the two most important reasons for hysteresis. Among various kinds of intrinsic defects, iodine vacancy V$_I$ is thought to play a major role in arousing the severe hysteresis of PSCs as it has a significant concentration[29] and a low migration energy barrier[21,24,30] in MAPbI$_3$ layer. When the applied electric field in PSCs changes in direction and strength, V$_I$ migrates between two contacts, leading to hysteresis, which affects the stability and PCE of MAPbI$_3$ PSCs.

MAPbI$_3$ are mostly in the form of thin films covering on mesoporous TiO$_2$ (or Al$_2$O$_3$) scaffolds,[31−33] or in the form of thin film p-i-n structures[34−36] in high-performance MAPbI$_3$ PSCs. Critical electron dynamic processes, such as the extraction of hot carriers and holes, charge transfer to the electron and hole transporters, electron−hole recombination, which directly determine the macroscopic properties and overall efficiency of PSCs, take place at the MAPbI$_3$/TiO$_2$ heterojunction interfaces. Although the nature of defects in bulk MAPbI$_3$ perovskite have been studied before,[37,38] the properties of surface and interfacial defects in MAPbI$_3$ PSCs and furthermore, how the defects in MAPbI$_3$ layer affect the interfacial electron dynamics, have not yet been studied systematically.

In this work, we study the structural and electronic properties of V$_I$ at different sites of MAPbI$_3$ PSCs. We found V$_I$ is most stable at the surface or interface. V$_I$ at the Pb−I layer and MA−I layer is quite different: V$_I$ at MA−I layer is more stable, while V$_I$ defect states at the Pb−I layer are more local and weakly covalent bonded. V$_I$ promotes both electronic injection and recombination rates, but overall reduces the PCE of PSCs. Additionally, the interfacial V$_I$ is found to be the least harmful

to the PCE of PSCs than the randomly distributed V_I in bulk, explaining the overall high performance of PSCs.

2. SIMULATION METHODOLOGY

First-principles calculations based on density functional theory (DFT) are performed with the ab initio VASP code.[39] Exchange-correlation functional of generalized gradient approximation (GGA) of Perdew, Burke, and Ernzerhof (PBE),[40] and pseudopotential of projector augmented wave (PAW)[41] are employed. The energy cutoff for plane waves is 500 eV.

For geometry optimization of bulk TiO_2 and perovskite, a 4 × 4 × 4 Monkhorst−Pack grid is chosen for sampling the Brillouin zone. The calculated lattice constants are $a = 6.3115$ Å and $c = 6.3161$ Å for bulk $MAPbI_3$ perovskite; $a = 4.66$ Å and $c = 3.00$ Å for bulk rutile-TiO_2. These values are in good agreement with the corresponding experimental ones ($a = 6.26$ Å and $c = 6.33$ Å for bulk perovskite;[42] $a = 4.59$ Å, and $c = 2.96$ Å for rutile-TiO_2). Our calculated energy gap of bulk $MAPbI_3$ is 1.67 eV, in good agreement with the experimental value of 1.57 eV,[43] due to the cancellation of errors in exchange-correlation functional and the neglect of spin orbital coupling (SOC). This cancellation also results in a small difference between the results of PBE and GW+SOC or HSE+SOC, verified by many other works on $MAPbI_3$.[37,44,45] In addition, we cannot afford such a huge computation cost for the large systems (over 200 atoms for both $MAPbI_3$ slab and $MAPbI_3/TiO_2$ heterojunction), especially for the nonadiabatic molecular dynamics simulations where thousands of electronic structure calculations are performed along the trajectories.

The Γ centered 2 × 2 × 1 Monkhorst−Pack grid is chosen for sampling the Brillouin zone in calculating the ground state properties of $MAPbI_3$ slab (Figure 1) and $MAPbI_3/TiO_2$
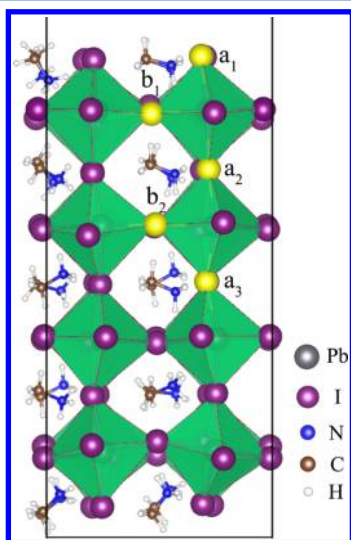
Figure 1. Atomic structure of the nine-layer $MAPbI_3$ perovskite slab. a_1, a_2, and a_3 denote iodine vacancies V_I located at the MA−I layers from surface to inner unit cell, and b_1 and b_2 denote V_I located at the Pb−I layers from surface to inner unit cell.

heterojunction (Figure 5a). For $MAPbI_3$ slab, the nine atomic layers of the halide perovskite has been used and periodic 2 × 2 supercell is adopted in the parallel X−Y plane. The thickness of the vacuum slab is 14 Å. For $MAPbI_3/TiO_2$ heterojunction, we choose the (110) facets of TiO_2 as the interface between perovskite and TiO_2 because of its good stability. A (2 × 4)

surface slab with 96 atoms in six atomic layers is used to model rutile-TiO_2, above which a (2 × 2) five-layer perovskite sheet in (001) direction containing another 132 atoms is included in the calculations. The thickness of the vacuum slab is 16 Å. There are lattice mismatches of 6.98% in X direction and 1.36% in Y direction. Ti atoms are right below the interfacial I atoms. The distance between $MAPbI_3$ and TiO_2 is fully relaxed.

The interfacial charge transfer dynamics are calculated using trajectory surface hopping method.[46−48] In nonadiabatic molecular dynamics (NAMD) simulations of the interfacial electron injection and electron−hole recombination processes, we first bring the system temperature to 300 K with velocity rescaling, then carry out molecular dynamics (MD) simulations in the microcanonical ensemble for 1 ps with the MD time step of 1 fs. The MD trajectory is subsequently used in the NAMD calculations. To determine interfacial charge transfer dynamics, 300 short MD trajectories each with 100 fs long for electron injection and 200 fs long for charge recombination are included in the ensemble average, the averaging turns out to be crucial for capturing the stochastic nature of the coupled electron−ion dynamics. For each trajectory, the time-dependent density functional theory (TDDFT) equation is integrated with a time step of 10^{-3} fs. For the interfacial electron injection dynamics, the initial photoexcited state is chosen from the low-lying empty states with the largest localization on the perovskite layer. On the other hand, for the electron−hole recombination dynamics, the conduction band minimum of TiO_2 is selected as the initial state for the electron while the hole is always sitting in the valence bands of the perovskite.

3. RESULTS AND DISCUSSION

3.1. Geometry and Stability of V_I in a $MAPbI_3$ Slab. The structure of nine-layer tetragonal $I4/mcm$ $MAPbI_3$ is shown in Figure 1. PbI_6 octahedra build up the framework of $MAPbI_3$ perovskite. MA organic molecules are located in the cages surrounded by PbI_6 octahedra, which are slightly rotated along Z axis. Previous works have investigated the stability of MA−I terminated and Pb−I terminated perovskite slabs, the surface energies of MA-I layers are found to be lower than that of Pb−I layers,[49] as the surface MA dipoles could weaken the surface polarity of perovskite and consequently stabilize the slab structures.[50,51] Hence, we choose symmetric MA−I layers as the termination surfaces for $MAPbI_3$ perovskite. The structure relaxation of $MAPbI_3$ slab starts with the initial structures that the C−N bonds of MA moieties are parallel to the X−Y surface. After relaxation, the C−N bonds are rotated so that the hydrogens in the MA molecules approach iodine atoms to form hydrogen bonds and stabilize the surface structure.[52] Five different sites of V_I are considered (the yellow spheres in Figure 1), which can be classified into two groups: V_I-a_1, V_I-a_2, and V_I-a_3 are located at the MA-I layers, and V_I-b_1 and V_I-b_2 are located at the Pb−I layers. On account of the fact that the distances of V_I-a_3 and V_I-b_2 from the surface are over 10 Å, they own similar properties of V_I in the bulk perovskite.

We have calculated the formation energy H_q of iodine vacancies at different surface and subsurface sites of $MAPbI_3$ slab. The formation energy H_q of a single iodine vacancy with charge q is defined as[53]

$$H_q(E_F, \mu_I) = (E_{defect}^q - E_{pristine}^q) + q(E_V + E_F) + \mu_I$$

(1)

where E_{defect}^q and $E_{pristine}^q$ are the free energies of a defective cell (with V_I) and a pristine cell with charge q, respectively.

Conditions of charge $q = -1$, 0, or 1 for V_I are considered. E_F is the Fermi level energy with respect to the valence band maximum (VBM) of TiO_2, which ranges from 0 to the band gap E_g. Energy of VBM E_V is set zero for positively charged V_I and $-E_g$ for negatively charged V_I. The reference chemical potential of iodine μ_I is set as $\mu_I = -1.683$ eV for I-poor limit and $\mu_I = -2.533$ eV for I-rich limit (the allowed regions of μ_I are between these two values).[37] Therefore, H_q is actually a function of E_F and μ_I.

Table 1 shows the calculated formation energies in I-poor limit and I-rich limit with $q = 0$. We can learn that all formation

Table 1. Formation Energies of V_I in Nine-Layer MAPbI$_3$ Slab with $q = 0$

formation energy	I-poor (eV)	I-rich (eV)
V_I-a_1	1.63	0.78
V_I-a_2	1.81	0.96
V_I-a_3	1.70	0.85
V_I-b_1	1.93	1.08
V_I-b_2	1.98	1.13

energies are smaller than 2 eV. The formation energies of a-type V_I are lower than that of b-type, indicating V_I at MA-I layers are more stable thermodynamically, which is due to the interatomic interactions of MA-I bond are weaker than that of Pb–I bond. Moreover, V_I-a_1 has the lowest formation energy, which means V_I prefers to reside at the surface of perovskite layer, consistent with the experimental observations that V_I accumulate at grain boundaries of MAPbI$_3$ PSCs.[13,54] It can be explained by the fact that removing an iodine needs to break less bonds at the surface than in the bulk material.

Figure 2 shows the formation energy H_q of iodine vacancy as a function of E_F and μ_I for both I-poor and I-rich conditions. For simplification, only results of V_I-a_1 (a-type at surface), V_I-a_3 (a-type in bulk), and V_I-b_1 (b-type) in I-poor conditions and I-rich conditions are shown. Cases of V_I-a_2 and V_I-b_2 are similar to these situations. Defect charge states from -1 to 1 are calculated. The crossovers at which two charge states share the same formation energies are the charge transition levels. Defect charge states would change at these energy levels. For n-type doping V_I, Fermi surfaces are right below the conduction band minimum (CBM) E_C of MAPbI$_3$, as shown in Figure 3b–f (red dashed lines). When the Fermi energy E_F gets close to E_C, the charge state of V_I changes from +1 to 0, indicating the most stable iodine vacancy V_I is mostly dominated by the $q = 0$ charge state in all cases. The case $q = 0$ is also the most stable charge state for V_I in bulk perovskite, and also for V_I-a_2 and V_I-b_2. So we only focus on the $q = 0$ charge state in the following discussion.

3.2. Electronic Properties of V_I in MAPbI$_3$ Slab. Electronic structures of V_I at different sites in the nine-layer MAPbI$_3$ slab with $q = 0$ are presented in Figure 3. Comparing with the energy band of the intact structure, we find that the defect states (denoted by red solid lines) contributed by the presence of V_I are right below the CBM E_C ($\sim$0.04 eV below E_C at G point for a-type V_I, and $\sim$0.2 eV below E_C at G point for b-type V_I) and around the Fermi energy E_F (red dashed lines) for all cases, indicating that these defect states are all half-filled. Obviously, the defect states of b-type V_I are more localized than that of a-type V_I. This can be further demonstrated by the partial charge densities of the defect states at the G point (Figure 4), which are mainly contributed
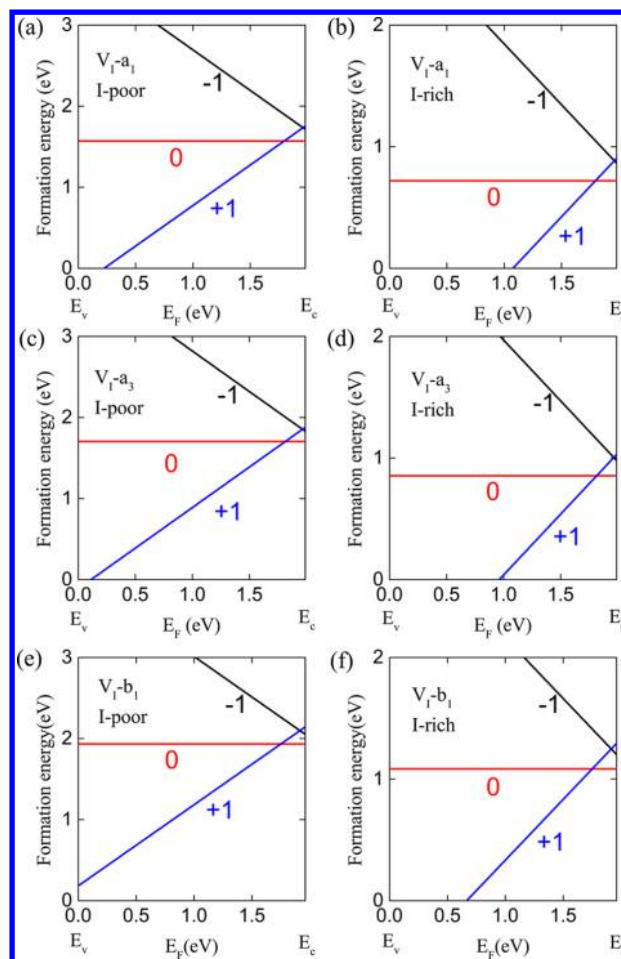
Figure 2. Formation energies of (a,b) V_I-a_1, (c,d) V_I-a_3, and (e,f) V_I-b_1 as a function of E_F and μ_I for nine-layer MAPbI$_3$ slab. The left column represents the I-poor limit, and the right column represents the I-rich limit. Energy of valence band maximum (VBM) E_V is set to zero. Fermi energy E_F ranges from E_V to conduction band minimum (CBM) E_C, or from 0 to the energy gap value E_g.

from Pb atoms. The free electrons provided by V_I are trapped by the surrounding Pb atoms, hence the charge density distributions of the structure with b-type V_I are mainly residing at in-plane Pb atoms and are more localized than that of a-type V_I. In Figure 4c, the distance between two Pb atoms adjacent to V_I-b_1 shrinks from 6.5 to 6.4 Å when V_I-b_1 is doped, meanwhile the charge densities of these two Pb atoms overlap with each other, forming a bonding-like charge state, revealing the formation of a Pb–Pb dimer. Our findings are consistent with the covalent features of V_I in bulk MAPbI$_3$ reported by Zhang et al.[37] Consequently, a-type V_I defect states are ionic, while b-type V_I defect states are more localized and weakly covalent-bonded.

3.3. Geometry and Stability of V_I in MAPbI$_3$/TiO$_2$ Heterojunction. Furthermore, to investigate the properties of iodine vacancies in MAPbI$_3$/TiO$_2$ heterojunctions, we add a rutile-TiO$_2$ slab below MAPbI$_3$ to form a heterojunction mimicking the functional interface in working perovskite solar cells, as shown in Figure 5a. We utilized a five-layer MAPbI$_3$ slab here in consideration of unaffordable computation cost for large supercells. Similarly, we choose symmetric MA-I layers as the termination surface and interface for MAPbI$_3$/TiO$_2$. Three different sites of iodine vacancies are considered here: V_I-a_1,
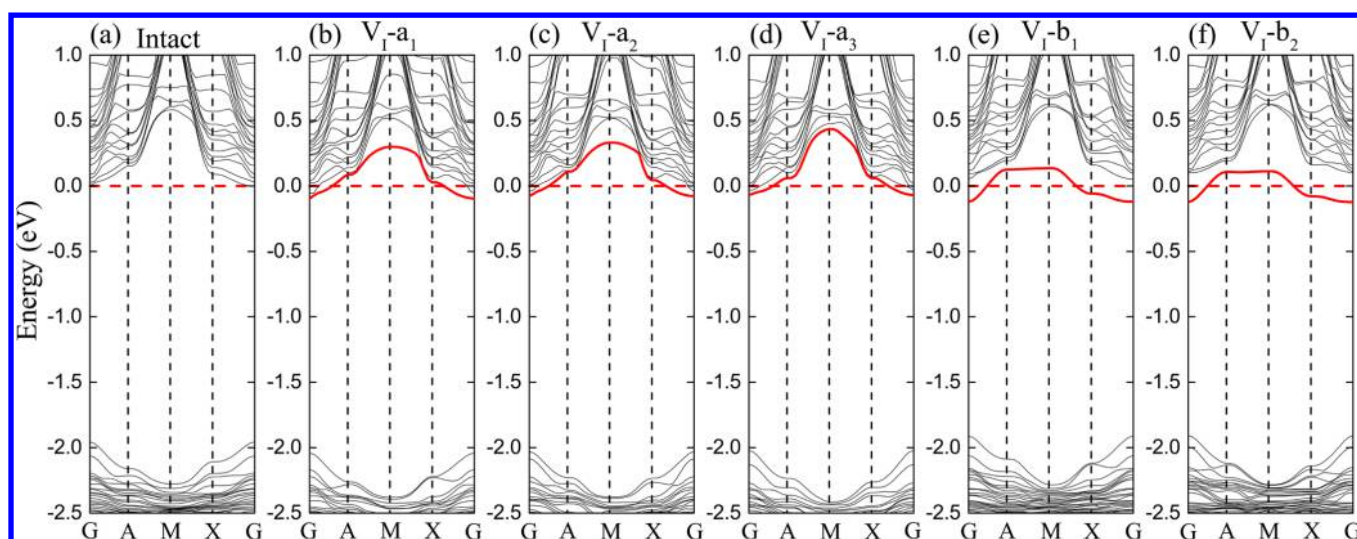
Figure 3. Energy bands for (a) intact structure and (b−f) structures with different sites of V_I in the nine-layer MAPbI$_3$ slab with $q = 0$. High symmetry routines are from G (0,0,0) to A(0.5,0,0) to M(0.5,0.5,0) to X(0,0.5,0), and then back to G. The energy gaps from a to f are 1.96 eV, 1.98 eV, 1.96 eV, 1.99 eV, 2.01 and 1.99 eV respectively, larger than that of bulk (1.67 eV) as a result of quantum size effect. Fermi energies are shown as red dashed lines. The red solid lines are energy bands of defect states.
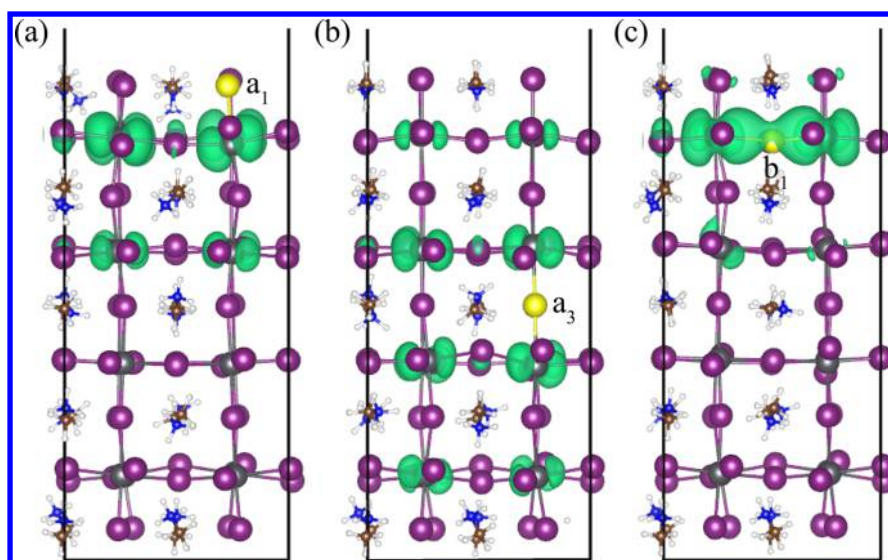
Figure 4. Partial charge densities of defect states for structures with (a) V_I-a_1, (b) V_I-a_3, and (c) V_I-b_1 at G(0,0,0) in the nine-layer MAPbI$_3$ slab with $q = 0$. Isosurface level is set to be 0.0007 e/Å^3. Three sites of iodine vacancies are shown in yellow spheres. Charge densities shown in green color are distributed on the corner-sharing octahedral frameworks, mainly around Pb atoms.

where the iodine vacancy is located at the interfacial MA-I layer; V_I-a_2 with V_I resided in the sub-MA-I layer of the MAPbI$_3$ slab; V_I-b_1 with V_I lay on the Pb−I atomic layer near the MAPbI$_3$/TiO$_2$ interface.

The formation energies of V_I in MAPbI$_3$/TiO$_2$ are in line with the results of V_I in the freestanding perovskite slab that a-type V_I in MAPbI$_3$/TiO$_2$ are also more stable than b-type V_I, meanwhile iodine vacancy at the MAPbI$_3$/TiO$_2$ interface (V_I-a_1) are more stable than bulk, implying that iodine vacancies in PSCs are mostly located at the heterojunction interface. Previous works show that the kinetic energy barrier for V_I migration in bulk MAPbI$_3$ is exceedingly low (several hundred meV),[21,24] and is even lower when V_I is close to the MAPbI$_3$ surface or MAPbI$_3$/TiO$_2$ interface, which can be overcome at room temperature. Therefore, V_I can be easily transferred to the perovskite surface or perovskite/TiO$_2$ interface, accumulat-

ing at the surface or interface in the thermodynamic equilibrium.

In MAPbI$_3$ PSCs, the current densities depend on the sweeping directions of applied bias, resulting in hysteresis. Based on our results, ion vacancies V_I accumulate at the interface of MAPbI$_3$/TiO$_2$, which is adjacent to the photoanode of MAPbI$_3$ PSCs device. The built-in electric field points away from the interface due to the asymmetrical work function of photocathode Au and photoanode TiO$_2$. Hence the negatively charged iodine ions in MAPbI$_3$ slab can migrate to the interfacial vacancy sites under the built-in electric field, and affect the generation and transport of photoexcited electrons. When sweeping a bias from short circuit condition to open circuit condition on both ends of MAPbI$_3$ PSCs device (i.e., forward sweep), the external electric field pointing to the interface increases, so the effective built-in electric field
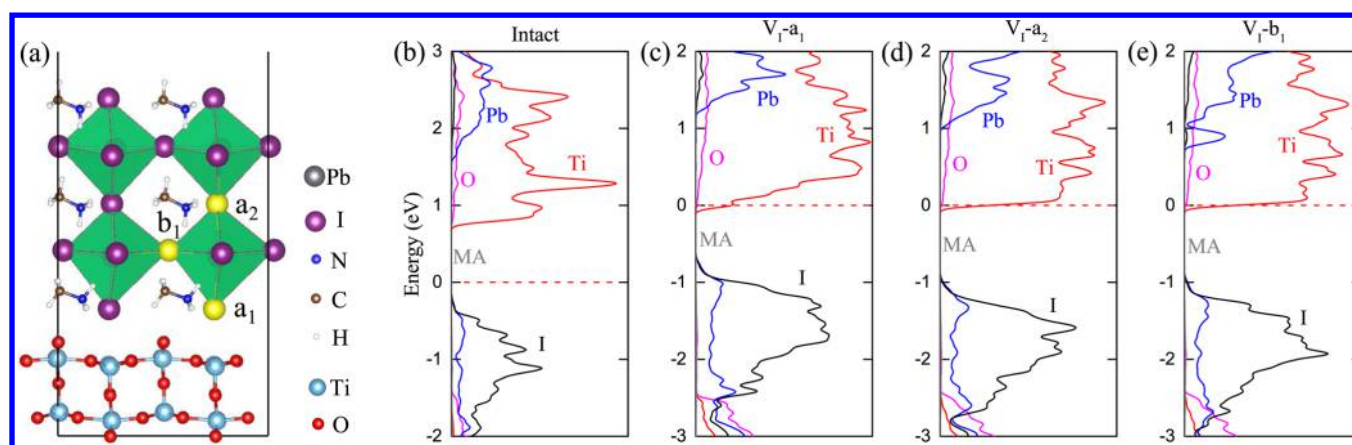
Figure 5. (a) Atomic structure of the MAPbI$_3$/TiO$_2$ heterojunction. Three sites of iodine vacancies are shown in yellow spheres. (b−e) The partial density of states (PDOS) of intact geometry and structures with three sites of iodine vacancies. Red and pink solid lines are the contributions of Ti and O atoms. Blue, black, and gray solid lines are the contributions of Pb, I atoms and MA molecules, respectively. The Fermi levels shown in red dashed lines are shifted about 1 eV in the presence of V$_I$.

Table 2. Energy Levels of HOMO, LUMO, VBM, CBM, and Injection Driving Force ΔG_{inj}, Injection Time Scale τ_{inj}, Recombination Driving Force ΔG_{rec}, Recombination Time Scale τ_{rec} of Four Structures (Abbreviated As Intact, V$_I$-a$_1$, V$_I$-a$_2$, and V$_I$-b$_1$)^a

	HOMO (eV)	LUMO (eV)	VBM (eV)	CBM (eV)	ΔG_{inj} (eV)	τ_{inj} (fs)	ΔG_{rec} (eV)	τ_{rec} (ps)
intact	−0.25	1.76	−1.07	0.78	0.98	7.57	1.03	507.08
V$_I$-a$_1$	−0.74	1.36	−2.45	−0.01	1.37	2.51	0.73	474.94
V$_I$-a$_2$	−1.00	1.12	−2.43	0.003	1.12	2.98	1.00	215.18
V$_I$-b$_1$	−1.00	1.14	−2.43	0.003	1.14	3.17	1.00	301.53

^{a}Injection driving force is defined as $\Delta G_{inj} = E_{LUMO} - E_{CBM}$, recombination driving force is defined as $\Delta G_{rec} = E_{CBM} - E_{HOMO}$.

decreases. However, when a bias from open circuit condition to short circuit condition (i.e., backward sweep) is applied, the effective built-in electric field increases. Hence the migration of iodine ions under forward sweep and backward sweep are different, resulting in different current densities of forward sweep and backward sweep,[19] which could contribute to hysteresis. Surface and interfacial accumulated V$_I$ can be pinned or passivated by inserting a phenyl-C61-butyric acid methyl ester (PCBM) layer between perovskite and photoanode[26,27,55] to eliminate ion migration processes and charge trapping and detrapping processes. Then the hysteresis will be suppressed, and the performances of PSCs will be improved.

3.4. Electronic Properties and Charge Transfer Dynamics of V$_I$ in MAPbI$_3$/TiO$_2$ Heterojunction. Figure 5b−e presents the partial density of states (PDOS) of intact MAPbI$_3$/TiO$_2$, as well as those with different sites of iodine vacancies. The PDOS is decomposed into contributions from Pb, I, MA, Ti and O species. It shows that the highest occupied molecular orbital (HOMO) of perovskite is composed mainly by I atoms, and the lowest unoccupied molecular orbital (LUMO) of perovskite is composed mainly from Pb atoms. MA molecules contribute little to the band edge states. Meanwhile the CBM of TiO$_2$ is consist mostly of Ti atoms, and VBM of TiO$_2$ is consist mostly of O atoms. The energy levels of HOMO, LUMO, VBM and CBM are shown in Table 2. The defect states of V$_I$-a$_1$ and V$_I$-a$_2$ are overwhelmed by the conduction bands of perovskite, while the defect state below LUMO contributed from Pb atoms for V$_I$-b$_1$ is clearly seen due to the locality of defect state of b-type V$_I$, as discussed in Figure 3 and Figure 4.

Interfacial electron injection and electron−hole recombination processes are two key factors that determine the overall

properties and performance of PSCs. Ultrafast electron injection from MAPbI$_3$ layer into TiO$_2$ semiconductor ensures efficient separation of electrons and holes at interface, thus reducing the energy and current losses of thermal relaxation. Injected electrons in TiO$_2$ slab recombine with holes in MAPbI$_3$ layer, triggering fluorescence, are another major pathway for charge and energy loss. Therefore, improving the injection efficiency and suppressing the electron−hole recombination can effectively optimize the perovskite photovoltaic devices.

To further look into how the iodine vacancy influence the particularly important electron injection and electron−hole recombination at the MAPbI$_3$/TiO$_2$ interface, we perform NAMD simulations of the two processes. The fraction of electron injection at a given time t can be determined by the amount (or the fraction) of the photoexcited electrons left on the perovskite region,[46−48]

$$\chi(t) = \sum_{i,j} c_i^*(t) c_j(t) \int_{perov} \phi_i^*(r, R(t)) \phi_j(r, R(t)) dr \tag{2}$$

where ϕ_i and ϕ_j are the adiabatic Kohn−Sham orbitals, $c_i(t)$ and $c_j(t)$ are the hopping probabilities from one adiabatic Kohn−Sham state to another, and r and $R(t)$ are the coordinates of electrons and atoms. The integration is over the volume of the MAPbI$_3$ perovskite. The time evolved charge transfer is given by

$$\frac{d}{dt}\chi(t) = \sum_{i,j} \left\{ \frac{dc_i^*(t)c_j(t)}{dt} \int_{perov} \phi_i^*(r, R(t))\phi_j(r, R(t))dr \right.$$

$$\left. + c_i^*(t)c_j(t) \frac{d\int_{perov}\phi_i^*(r, R(t))\phi_j(r, R(t))dr}{dt} \right\}$$

(3)

Here, the first term on the right side represents the contribution of nonadiabatic charge transfer, where charge transfer is accomplished by photoexcited electron's hopping from one state to another. The second term is the contribution of adiabatic charge transfer, where charge transfer is done by Kohn−Sham orbital where photoexcited electron occupied evolving in space. Similarly, the charge transfer of recombination at a given time t can be determined by the fraction of the photoexcited electrons remaining at TiO_2, which also involves the contributions of nonadiabatic and adiabatic charge transfer.

Figure 6a shows the fraction of electrons injected from the perovskite to TiO_2 conduction bands for intact structure and in
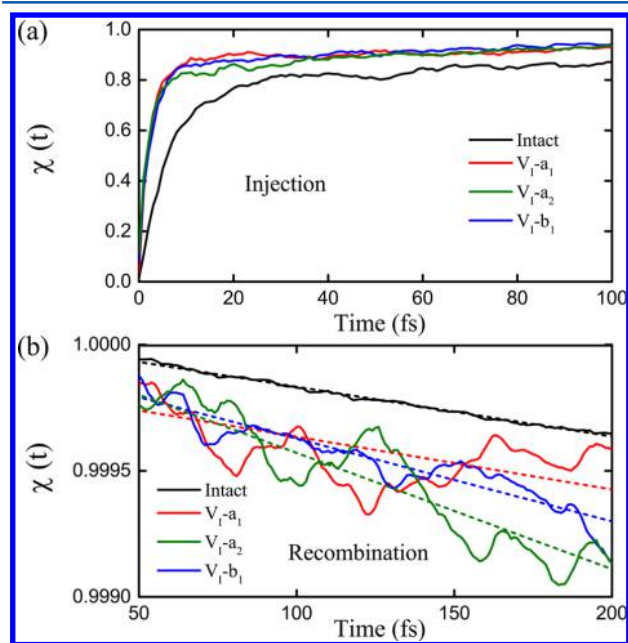
Figure 6. (a) The fraction of interfacial injection charge transfer as a function of time. (b) The fraction of interfacial recombination charge transfer as a function of time.

the presence of different V_I sites. By exponentially fitting $\chi(t)$, the fraction of photoexcited electron transfer, with the equation $\chi_1(t) = \chi_f(1 - \exp[-k(t - t_0)])$, we obtain the injection time scales of intact $MAPbI_3/TiO_2$, as well as those with different sites of V_I (Table 2). Here χ_f is the final amount of charge transfer, and k is the estimated electron injection rate. Due to the electronic coupling between perovskite and TiO_2 electrode, there is always a small fraction of the photoexcited state residing at TiO_2 at t_0, which can be interpreted as the charge transfer time corresponding to the pretransferred amount. The injection time scale $\tau_{inj} = 1/k$, is estimated to be 7.57 fs for intact structure, 2.51 fs for the structure with V_I-a_1, 2.98 fs for that with V_I-a_2, and 3.17 fs for that with V_I-b_1, respectively. All the structures display ultrafast electron injection into TiO_2 within 10 fs, indicating high electron injection efficiency of

relevant PSCs. Interestingly, compared with the intact geometry, structures with iodine vacancy possess 2−3 times faster injection dynamics, which means V_I promotes the injection rates in $MAPbI_3$ PSCs, meanwhile the structure with V_I-a_1 possesses the shortest injection time. These can be explained by injection energy driving forces from the energy difference of LUMO and CBM: $\Delta G_{inj} = E_{LUMO} - E_{CBM}$ (Table 2). The largest ΔG_{inj} (1.37 eV) leads to the shortest τ_{inj} (2.51 fs) for the structure with V_I-a_1, while the smallest ΔG_{inj} (0.98 eV) leads to the longest τ_{inj} (7.57 fs) for intact structure.

The electron−hole recombination dynamics for all above structures are shown in Figure 6b. Similarly, by linear fitting $\chi(t)$ of the recombination process with the equation $\chi_2(t) = a + bt$, we get the recombination time scales $\tau_{rec} = -a/b$, where a is the initial amount of photoexcited electrons at TiO_2 and b is the estimated electron recombination rate. Recombination time scales are estimated to be 507.08 ps for intact structure, 474.94 ps for the structure with V_I-a_1, 215.18 ps for that with V_I-a_2, and 301.53 ps for that with V_I-b_1, respectively (Table 2). It manifests that the recombination processes are very slow for all the structures. Surprisingly, the recombination process of the structure with V_I-a_1 is slower than that of other sites of V_I due to its smaller energy driving force of recombination (0.73 eV for that with V_I-a_1, and 1.00 eV for that with V_I-a_2 and V_I-b_1), which comes from the energy difference of CBM and HOMO: $\Delta G_{rec} = E_{CBM} - E_{HOMO}$. However, the intact structure possesses the longest recombination time scale regardless of its largest recombination driving force. This can be explained by the fact that, according to Marcus theory,[56] the electron dynamics are also determined by several other factors, such as the distances between perovskite and TiO_2 and electronic couplings of initial (CBM) and final (HOMO) states. The distances between perovskite and TiO_2 for four structures are extremely close (around 4.6 Å), meanwhile the partial charge densities of CBM are also exceedingly similar and mainly residing at Ti atoms. But the partial charge densities of HOMO (shown in Figure 7) are quite different. It seems that charge densities of HOMO contributed from iodine atoms are repulsed both by TiO_2 and V_I. Thus, for intact heterostructure, charge densities of HOMO are far away from TiO_2, which means the electronic couplings of HOMO and CBM are small, resulting in a long τ_{rec} (507.08 ps). Oppositely, for that with V_I-a_2, charge densities of HOMO are very close to TiO_2, giving rise to a large electronic coupling and a short τ_{rec} (215.18 ps).

Comparing τ_{inj} and τ_{rec} among four structures, we can see the following: (1) Injection time scales and recombination time scales of the structures with V_I are all shorter than or equal to that of intact structure. That is to say, the existence of V_I promotes both injection and recombination rates in PSCs. However, the injections are very fast and complete, while the recombinations are slow (several hundred picoseconds). The influences of V_I on recombination rates would be relatively more important and remarkable. Additionally, we note that the recombination time scale is closely related to the recombination resistance,[57] $R_0 \propto 1/k_{rec} = \tau_{rec}$, where k_{rec} is the recombination rate. The recombination resistance would then dramatically influence the open circuit voltage V_{OC} and the overall PCE. Longer τ_{rec} comparing to the carrier transport time τ_{tran} also favors a larger short circuit current density $J_{SC} \propto \tau_{rec}/\tau_{tran}$. Although the same order of magnitude for the recombination time scale is obtained here for pristine and defective interfaces, a tremendous change in PCE can be resulted with a small variation in τ_{rec}. So, overall, the existence of V_I would reduce
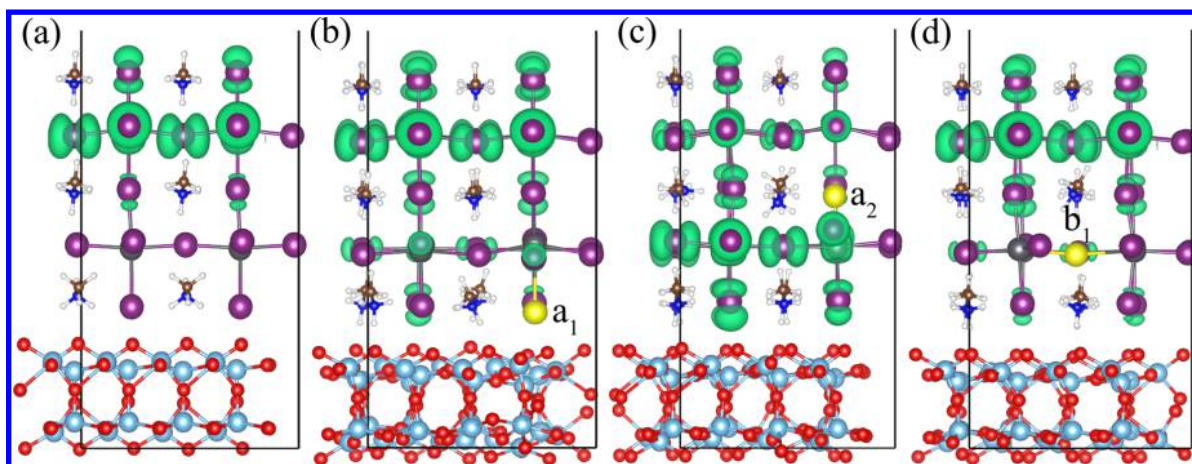
Figure 7. Partial charge density distribution of the HOMO of perovskite layer for (a) intact structure and (b−d) structures with V_I-a_1, V_I-a_2, and V_I-b_1, respectively. Isosurface level is set to be 0.0005 e/$Å^3$. Three sites of iodine vacancies are shown in yellow spheres.

the PCE of PSCs. (2) Among the structures with various sites of V_I, the structure with V_I-a_1 has the shortest τ_{inj} and longest τ_{rec}. In other words, V_I accumulating at the $MAPbI_3$/TiO_2 interface does the least harm to the overall performance and the PCE of PSCs, as compared to the cases of V_I randomly distributed in the bulk.

4. CONCLUSION

In conclusion, we use the extensive first-principles calculations and nonadiabatic electron dynamics simulations to study the properties of iodine vacancies V_I at different sites of freestanding $MAPbI_3$ film and the $MAPbI_3$/TiO_2 heterojunction. Our results indicate that

(i) V_I at surface ($MAPbI_3$) and interfacial ($MAPbI_3$/TiO_2) MA-I layer are most stable comparing with random sites in the bulk. Consequently, V_I's prefer to accumulate at surfaces or interfaces in the thermodynamic equilibrium, consistent with the accumulation of V_I at grain boundaries of $MAPbI_3$ PSCs observed in experiments. V_I's accumulating at interfaces and migrating in the perovskite layer under electric field during voltage scans leads to hysteresis.

(ii) V_I at Pb−I layer and MA−I layer are quite different. V_I at MA−I layer are more stable, while V_I defect states at Pb−I layer are more local and weakly covalent-bonded.

(iii) V_I promotes both electronic injection and recombination rates of $MAPbI_3$ PSCs, but overall reduces the PCE of PSCs. Most important of all, interfacial V_I is found to be the least harmful to the PCE of PSCs comparing with bulk sites, which could be responsible for the high PCE of $MAPbI_3$ PSCs.

The analyses of V_I in $MAPbI_3$ PSCs provide systematic and detailed explanations of the stability, anomalous hysteresis and high PCE of PSCs. Our studies construct an unambiguous link between the microscopic interfacial structures and macroscopic photovoltaic properties of PSCs, and pave the way for innovative solar cell design and optimization.

■ AUTHOR INFORMATION

Corresponding Author
*E-mail: smeng@iphy.ac.cn.

ORCID ⊙
Chao Lian: 0000-0002-2583-9334

Sheng Meng: 0000-0002-1553-1432

Author Contributions
§Contributed equally to this work

Notes
The authors declare no competing financial interest.

■ ACKNOWLEDGMENTS

■ REFERENCES

(1) Bi, D.; Tress, W.; Dar, M. I.; Gao, P.; Luo, J.; Renevier, C.; Schenk, K.; Abate, A.; Giordano, F.; Baena, J.-P. C.; et al. Efficient luminescent solar cells based on tailored mixed-cation perovskites. *Science Advances* **2016**, *2*, e1501170.

(2) Saliba, M.; Matsui, T.; Seo, J.-Y.; Domanski, K.; Correa-Baena, J.-P.; Nazeeruddin, M. K.; Zakeeruddin, S. M.; Tress, W.; Abate, A.; Hagfeldt, A.; et al. Cesium-containing triple cation perovskite solar cells: improved stability, reproducibility and high efficiency. *Energy Environ. Sci.* **2016**, *9*, 1989−1997.

(3) Snaith, H. J. Perovskites: the emergence of a new era for low-cost, high-efficiency solar cells. *J. Phys. Chem. Lett.* **2013**, *4*, 3623−3630.

(4) Burschka, J.; Pellet, N.; Moon, S.-J.; Humphry-Baker, R.; Gao, P.; Nazeeruddin, M. K.; Grätzel, M. Sequential deposition as a route to high-performance perovskite-sensitized solar cells. *Nature* **2013**, *499*, 316−319.

(5) Chen, W.; Wu, Y.; Yue, Y.; Liu, J.; Zhang, W.; Yang, X.; Chen, H.; Bi, E.; Ashraful, I.; Grätzel, M.; et al. Efficient and stable large-area perovskite solar cells with inorganic charge extraction layers. *Science* **2015**, *350*, 944−948.

(6) Grätzel, M. The light and shade of perovskite solar cells. *Nat. Mater.* **2014**, *13*, 838−842.

(7) Egger, D. A.; Edri, E.; Cahen, D.; Hodes, G. Perovskite solar cells: Do we know what we do not know? *J. Phys. Chem. Lett.* **2015**, *6*, 279−282.

(8) Xing, G.; Mathews, N.; Sun, S.; Lim, S. S.; Lam, Y. M.; Grätzel, M.; Mhaisalkar, S.; Sum, T. C. Long-range balanced electron-and hole-transport lengths in organic-inorganic $CH_3NH_3PbI_3$. *Science* **2013**, *342*, 344−347.

(9) Gonzalez-Pedro, V.; Juarez-Perez, E. J.; Arsyad, W.-S.; Barea, E. M.; Fabregat-Santiago, F.; Mora-Sero, I.; Bisquert, J. General working

principles of $CH_3NH_3PbX_3$ perovskite solar cells. *Nano Lett.* **2014**, *14*, 888−893.

(10) Zhou, H.; Chen, Q.; Li, G.; Luo, S.; Song, T.-b.; Duan, H.-S.; Hong, Z.; You, J.; Liu, Y.; Yang, Y. Interface engineering of highly efficient perovskite solar cells. *Science* **2014**, *345*, 542−546.

(11) Xing, G.; Mathews, N.; Lim, S. S.; Yantara, N.; Liu, X.; Sabba, D.; Grätzel, M.; Mhaisalkar, S.; Sum, T. C. Low-temperature solution-processed wavelength-tunable perovskites for lasing. *Nat. Mater.* **2014**, *13*, 476−480.

(12) Green, M. A.; Jiang, Y.; Soufiani, A. M.; Ho-Baillie, A. Optical properties of photovoltaic organic-inorganic lead halide perovskites. *J. Phys. Chem. Lett.* **2015**, *6*, 4774−4785.

(13) Tian, Y.; Merdasa, A.; Unger, E.; Abdellah, M.; Zheng, K.; McKibbin, S.; Mikkelsen, A.; Pullerits, T.; Yartsev, A.; Sundström, V.; et al. Enhanced organo-metal halide perovskite photoluminescence from nanosized defect-free crystallites and emitting sites. *J. Phys. Chem. Lett.* **2015**, *6*, 4171−4177.

(14) Matsumoto, F.; Vorpahl, S. M.; Banks, J. Q.; Sengupta, E.; Ginger, D. S. Photodecomposition and morphology evolution of organometal halide perovskite solar cells. *J. Phys. Chem. C* **2015**, *119*, 20810−20816.

(15) Labram, J. G.; Fabini, D. H.; Perry, E. E.; Lehner, A. J.; Wang, H.; Glaudell, A. M.; Wu, G.; Evans, H.; Buck, D.; Cotta, R.; et al. Temperature-dependent polarization in field-effect transport and photovoltaic measurements of methylammonium lead iodide. *J. Phys. Chem. Lett.* **2015**, *6*, 3565−3571.

(16) Carignano, M. A.; Kachmar, A.; Hutter, J. Thermal effects on $CH_3NH_3PbI_3$ perovskite from ab initio molecular dynamics simulations. *J. Phys. Chem. C* **2015**, *119*, 8991−8997.

(17) Christians, J. A.; Miranda Herrera, P. A.; Kamat, P. V. Transformation of the excited state and photovoltaic efficiency of $CH_3NH_3PbI_3$ perovskite upon controlled exposure to humidified air. *J. Am. Chem. Soc.* **2015**, *137*, 1530−1538.

(18) Li, D.; Bretschneider, S. A.; Bergmann, V. W.; Hermes, I. M.; Mars, J.; Klasen, A.; Lu, H.; Tremel, W.; Mezger, M.; Butt, H.-J.; et al. Humidity-induced grain boundaries in $MAPbI_3$ perovskite films. *J. Phys. Chem. C* **2016**, *120*, 6363−6368.

(19) Snaith, H. J.; Abate, A.; Ball, J. M.; Eperon, G. E.; Leijtens, T.; Noel, N. K.; Stranks, S. D.; Wang, J. T.-W.; Wojciechowski, K.; Zhang, W. Anomalous hysteresis in perovskite solar cells. *J. Phys. Chem. Lett.* **2014**, *5*, 1511−1515.

(20) Kim, H.-S.; Park, N.-G. Parameters affecting I−V hysteresis of $CH_3NH_3PbI_3$ perovskite solar cells: effects of perovskite crystal size and mesoporous TiO_2 layer. *J. Phys. Chem. Lett.* **2014**, *5*, 2927−2934.

(21) Haruyama, J.; Sodeyama, K.; Han, L.; Tateyama, Y. First-principles study of ion diffusion in perovskite solar cell sensitizers. *J. Am. Chem. Soc.* **2015**, *137*, 10048−10051.

(22) van Reenen, S.; Kemerink, M.; Snaith, H. J. Modeling anomalous hysteresis in perovskite solar cells. *J. Phys. Chem. Lett.* **2015**, *6*, 3808−3814.

(23) Sharma, P.; Gruverman, A.; Huang, J. Giant switchable photovoltaic effect in organometal trihalide perovskite devices. *Nat. Mater.* **2015**, *14*, 193−198.

(24) Eames, C.; Frost, J. M.; Barnes, P. R.; O'Regan, B. C.; Walsh, A.; Islam, M. S. Ionic transport in hybrid lead iodide perovskite solar cells. *Nat. Commun.* **2015**, *6*, 7497.

(25) Chen, B.; Yang, M.; Zheng, X.; Wu, C.; Li, W.; Yan, Y.; Bisquert, J.; Garcia-Belmonte, G.; Zhu, K.; Priya, S. Impact of capacitive effect and ion migration on the hysteretic behavior of perovskite solar cells. *J. Phys. Chem. Lett.* **2015**, *6*, 4693−4700.

(26) Shao, Y.; Xiao, Z.; Bi, C.; Yuan, Y.; Huang, J. Origin and elimination of photocurrent hysteresis by fullerene passivation in $CH_3NH_3PbI_3$ planar heterojunction solar cells. *Nat. Commun.* **2014**, *5*, 5784.

(27) Xu, J.; Buin, A.; Ip, A. H.; Li, W.; Voznyy, O.; Comin, R.; Yuan, M.; Jeon, S.; Ning, Z.; McDowell, J. J.; et al. Perovskite-fullerene hybrid materials suppress hysteresis in planar diodes. *Nat. Commun.* **2015**, *6*, 7081.

(28) Heo, J. H.; You, M. S.; Chang, M. H.; Yin, W.; Ahn, T. K.; Lee, S.-J.; Sung, S.-J.; Kim, D. H.; Im, S. H. Hysteresis-less mesoscopic $CH_3NH_3PbI_3$ perovskite hybrid solar cells by introduction of Li-treated TiO_2 electrode. *Nano Energy* **2015**, *15*, 530−539.

(29) Walsh, A.; Scanlon, D. O.; Chen, S.; Gong, X.; Wei, S.-H. Self-regulation mechanism for charged point defects in hybrid halide perovskites. *Angew. Chem.* **2015**, *127*, 1811−1814.

(30) Azpiroz, J. M.; Mosconi, E.; Bisquert, J.; De Angelis, F. Defect migration in methylammonium lead iodide and its role in perovskite solar cell operation. *Energy Environ. Sci.* **2015**, *8*, 2118−2127.

(31) Lee, M. M.; Teuscher, J.; Miyasaka, T.; Murakami, T. N.; Snaith, H. J. Efficient hybrid solar cells based on meso-superstructured organometal halide perovskites. *Science* **2012**, *338*, 643−647.

(32) Jeon, N. J.; Noh, J. H.; Kim, Y. C.; Yang, W. S.; Ryu, S.; Seok, S. I. Solvent engineering for high-performance inorganic−organic hybrid perovskite solar cells. *Nat. Mater.* **2014**, *13*, 897−903.

(33) Lee, Y. H.; Luo, J.; Son, M.-K.; Gao, P.; Cho, K. T.; Seo, J.; Zakeeruddin, S. M.; Grätzel, M.; Nazeeruddin, M. K. Enhanced charge collection with passivation layers in perovskite solar cells. *Adv. Mater.* **2016**, *28*, 3966−3972.

(34) Liu, M.; Johnston, M. B.; Snaith, H. J. Efficient planar heterojunction perovskite solar cells by vapour deposition. *Nature* **2013**, *501*, 395−398.

(35) Pascoe, A. R.; Duffy, N. W.; Scully, A. D.; Huang, F.; Cheng, Y.-B. Insights into planar $CH_3NH_3PbI_3$ perovskite solar cells using impedance spectroscopy. *J. Phys. Chem. C* **2015**, *119*, 4444−4453.

(36) Feng, H.-J.; Paudel, T. R.; Tsymbal, E. Y.; Zeng, X. C. Tunable optical properties and charge separation in $CH_3NH_3Sn_xPb_{1−x}I_3/TiO_2$-based planar perovskites cells. *J. Am. Chem. Soc.* **2015**, *137*, 8227−8236.

(37) Agiorgousis, M. L.; Sun, Y.-Y.; Zeng, H.; Zhang, S. Strong covalency-induced recombination centers in perovskite solar cell material $CH_3NH_3PbI_3$. *J. Am. Chem. Soc.* **2014**, *136*, 14570−14575.

(38) Song, D.; Cui, P.; Wang, T.; Wei, D.; Li, M.; Cao, F.; Yue, X.; Fu, P.; Li, Y.; He, Y.; et al. Managing carrier lifetime and doping property of lead halide perovskite by postannealing processes for highly efficient perovskite solar cells. *J. Phys. Chem. C* **2015**, *119*, 22812−22819.

(39) Kresse, G.; Furthmüller, J. Efficient iterative schemes for ab initio total-energy calculations using a plane-wave basis set. *Phys. Rev. B: Condens. Matter Mater. Phys.* **1996**, *54*, 11169.

(40) Perdew, J. P.; Burke, K.; Ernzerhof, M. Generalized gradient approximation made simple. *Phys. Rev. Lett.* **1996**, *77*, 3865.

(41) Kresse, G.; Joubert, D. From ultrasoft pseudopotentials to the projector augmented-wave method. *Phys. Rev. B: Condens. Matter Mater. Phys.* **1999**, *59*, 1758.

(42) Poglitsch, A.; Weber, D. Dynamic disorder in methylammoniumtrihalogenoplumbates (II) observed by millimeter-wave spectroscopy. *J. Chem. Phys.* **1987**, *87*, 6373−6378.

(43) Qiu, J.; Qiu, Y.; Yan, K.; Zhong, M.; Mu, C.; Yan, H.; Yang, S. All-solid-state hybrid solar cells based on a new organometal halide perovskite sensitizer and one-dimensional TiO_2 nanowire arrays. *Nanoscale* **2013**, *5*, 3245−3248.

(44) Umari, P.; Mosconi, E.; De Angelis, F. Relativistic GW calculations on $CH_3NH_3PbI_3$ and $CH_3NH_3SnI_3$ perovskites for solar cell applications. *Sci. Rep.* **2014**, *4*, 4467.

(45) Menéndez-Proupin, E.; Palacios, P.; Wahnón, P.; Conesa, J. Self-consistent relativistic band structure of the $CH_3NH_3PbI_3$ perovskite. *Phys. Rev. B: Condens. Matter Mater. Phys.* **2014**, *90*, 045207.

(46) Craig, C. F.; Duncan, W. R.; Prezhdo, O. V. Trajectory surface hopping in the time-dependent Kohn-Sham approach for electron-nuclear dynamics. *Phys. Rev. Lett.* **2005**, *95*, 163001.

(47) Li, Z.; Zhang, X.; Lu, G. Electron dynamics in dye-sensitized solar cells: Effects of surface terminations and defects. *J. Phys. Chem. B* **2010**, *114*, 17077−17083.

(48) Li, Z.; Zhang, X.; Lu, G. Dipole-assisted charge separation in organic-inorganic hybrid photovoltaic heterojunctions: insight from first-principles simulations. *J. Phys. Chem. C* **2012**, *116*, 9845−9851.

(49) Geng, W.; Tong, C.-J.; Tang, Z.-K.; Yam, C.; Zhang, Y.-N.; Lau, W.-M.; Liu, L.-M. Effect of surface composition on electronic properties of methylammonium lead iodide perovskite. *J. Materiomics* **2015**, *1*, 213−220.

(50) She, L.; Liu, M.; Zhong, D. Atomic structures of CH₃NH₃PbI₃ (001) surfaces. *ACS Nano* **2016**, *10*, 1126−1131.

(51) Wang, Y.; Sumpter, B. G.; Huang, J.; Zhang, H.; Liu, P.; Yang, H.; Zhao, H. Density functional studies of stoichiometric surfaces of orthorhombic hybrid perovskite CH₃NH₃PbI₃. *J. Phys. Chem. C* **2015**, *119*, 1136−1145.

(52) Long, R.; Liu, J.; Prezhdo, O. V. Unravelling the effects of grain boundary and chemical doping on electron-hole recombination in CH₃NH₃PbI₃ perovskite by time-domain atomistic simulation. *J. Am. Chem. Soc.* **2016**, *138*, 3884−3890.

(53) Li, H.; Guo, Y.; Robertson, J. Calculation of TiO₂ surface and subsurface oxygen vacancy by the screened exchange functional. *J. Phys. Chem. C* **2015**, *119*, 18160−18166.

(54) Nie, W.; Tsai, H.; Asadpour, R.; Blancon, J.-C.; Neukirch, A. J.; Gupta, G.; Crochet, J. J.; Chhowalla, M.; Tretiak, S.; Alam, M. A.; et al. High-efficiency solution-processed perovskite solar cells with millimeter-scale grains. *Science* **2015**, *347*, 522−525.

(55) Kim, H.-S.; Jang, I.-H.; Ahn, N.; Choi, M.; Guerrero, A.; Bisquert, J.; Park, N.-G. Control of I−V hysteresis in CH₃NH₃PbI₃ perovskite solar cell. *J. Phys. Chem. Lett.* **2015**, *6*, 4633−4639.

(56) Marcus, R. A. On the theory of electron-transfer reactions. VI. Unified treatment for homogeneous and electrode reactions. *J. Chem. Phys.* **1965**, *43*, 679−701.

(57) Ma, W.; Jiao, Y.; Meng, S. Predicting energy conversion efficiency of dye solar cells from first principles. *J. Phys. Chem. C* **2014**, *118*, 16447−16457.